Check for updates

The influence of strain on the properties of the FAPbI₃ photoactive phase†

Jiaqi Dai, [iD] [ab] Tingfeng Li,[ab] Xiaolei Li,[ab] Cuiping Xu,[ab] Min Zhao,[ab] Hongling Cai [iD] [ab] and Xiaoshan Wu*[ab]

Here the optoelectronic, defect, and mechanical properties of strain-induced α-FAPbI₃ are investigated. The strain range of −5% to 5% induces bandgap variation from 0.98 eV to 1.91 eV, and the strain along the [111] crystal orientation maintains a direct bandgap, while the strain along the [100] and [110] orientations may transform the direct bandgap into an indirect bandgap. Compressive strain shifts the iodine vacancy energy from the deep level to a shallow one, which stabilizes the photoactive material by elevating the α-FAPbI₃ phase. The [111] orientation under −2% strain achieves a photoelectric conversion efficiency (PCE) of 31.9%, providing an optimized strategy for designing efficient and stable perovskite solar cells.

1. Introduction

In recent years, organic–inorganic hybrid perovskites (OIHPs) have emerged as promising materials for photovoltaics due to their high power conversion efficiency (PCE),[1–3] broad spectral absorption,[4–6] long carrier diffusion lengths,[7] and versatile chemical tunability.[8,9] Single-junction OIHP solar cells now achieve PCEs exceeding 26%, while the PCEs of tandem architectures theoretically reach 33%.[10,11] However, their practical applications face challenges from structural degradation under light, humidity, and mechanical stress. For instance, the photoactive cubic phase of formamidinium lead iodide (NH₂CHNH₂PbI₃, α-FAPbI₃) readily transforms into a non-photoactive hexagonal phase (δ-FAPbI₃) at room temperature, leading to performance decay.[12–18] Residual lattice strain during fabrication, identified as a key instability factor,[19] arises from interfacial lattice and thermal expansion mismatch between perovskite films and substrates, resulting in coupled in-plane compressive and out-of-plane tensile strains.[20–22] To address this, strategies such as low-temperature annealing, flexible substrate matching, and solvent engineering have been proposed. For instance, Yang et al.[23] demonstrated that high-boiling solvents (e.g., DMF, DMSO) induce tensile strain via lattice contraction, whereas low-boiling solvents (e.g., isopropyl acetate) decelerate crystallization kinetics to mitigate strain accumulation.

Notably, strain exerts dual effects on perovskites. On one hand, residual strain can exacerbate lattice degradation under UV irradiation and shows close correlation with photoinduced phase segregation.[24–27] On the other hand, strain engineering enables proactive regulation of material properties. For example, Li et al.[28] found that cyclic lattice expansion and contraction under light and temperature fluctuations generate deep-level defects, which are stabilized by phenylselenyl chloride (Ph–Se–Cl) surface modification, extending device lifetimes tenfold. Similarly, Zheng et al.[25] utilized Rb⁺ doping combined with Cl⁻ to achieve uniform cation distribution and suppress phase separation through strain regulation. Additionally, the soft lattice nature of perovskites allows strain to modulate bandgap and carrier transport.[14,29] For example, Yin et al.[30] applied 2.7 GPa pressure to ⟨110⟩-oriented 2D perovskites, increasing octahedral distortion and boosting exciton mobility to 93.6 cm V⁻¹ s⁻¹. Wang and colleagues[31] reduced the bandgap of lead-free MA₃Sb₂I₉ from 2.43 eV to 1.64 eV under high pressure, observing a shift from ionic–electronic hybrid conduction to purely electronic conduction. Subbiah et al.[32] further demonstrated that solvent engineering reduces lattice strain (0.81%) and surface defect density (2.29 × 10⁹ cm⁻²) in FA₀.₈₂MA₀.₁₁Cs₀.₀₇ perovskites, achieving high hole mobility (77.58 cm² V⁻¹ s⁻¹). These findings highlight the profound impact of strain on perovskite properties. Despite these advances, systematic studies on strain effects in FAPbI₃ remain limited. Previous theoretical work, such as DFT calculations by Mahajabin et al.[33] and non-adiabatic molecular dynamics (NAMD) simulations by Ma et al.,[34] primarily links strain to bandgap modulation and non-radiative recombination but overlooks interactions between defects (e.g., iodine interstitials) and mechanical properties. This study employs first-principles

a National laboratory of Solid State Microstructures & Department of Physics, Nanjing University, Nanjing 210093, China. E-mail: xswu@nju.edu.cn

b Institute of Materials Engineering, Nantong 226019, China

† Electronic supplementary information (ESI) available. See DOI: https://doi.org/10.1039/d5cp02025e

DFT calculations to comprehensively investigate axial strain (−5% to 5%) effects on the optoelectronic properties, defect behavior, and mechanical performance of α-FAPbI$_3$. The results provide a theoretical foundation for mechano-optoelectronic co-design of FAPbI$_3$-based photovoltaics, advancing strain engineering for high-efficiency and stable perovskite solar cells.

2. Calculation methods

All calculations were performed using the Vienna *ab initio* Simulation Package (VASP)[35,36] with projector augmented wave (PAW) pseudopotentials.[37] The exchange–correlation functional was approximated by generalized gradient approximation (GGA) parameterized by Perdew–Burke–Ernzerhof (PBE).[38] A plane-wave energy cutoff of 600 eV and a Γ-centered $5 \times 5 \times 5$ k-point grid were utilized. Structural relaxations were conducted until forces on atoms fell below 0.03 eV Å^{-1} and the energy convergence reached 1×10^{-5} eV. To account for van der Waals interactions, the rev-vdW-DF2 functional proposed by Hamada[39] was employed, ensuring full optimization of atomic positions and lattice parameters. For accurate electronic structure analysis, ground-state geometries obtained from DFT were further refined using the GW method to compute quasiparticle energies and bandgaps.[40–42] For systems containing heavy elements, it is essential to consider the spin–orbit coupling (SOC) effect. Optical properties were evaluated by solving the Bethe–Salpeter equation (BSE)[43,44] based on GW results. Data extraction and post-processing were performed using VASPKIT.[45]

3. Crystal structure

The initial structure of FAPbI$_3$ was constructed using experimentally reported perovskite geometries.[46,47] As shown in Fig. 1, α-FAPbI$_3$ has a $Pm\bar{3}m$ space group with lattice parameters $a = b = c = 6.36$ Å. δ-FAPbI$_3$ has a $P6_3/m$ space group with lattice parameters $a = b = 8.507$ Å, $c = 7.591$ Å. Full structural relaxation was performed to optimize atomic positions and lattice constants. Previous studies indicate that perovskite single crystals exhibit exceptional deformability under mechanical strain (up to 30% compression), maintaining structural integrity due to multiple slip systems, low slip energy barriers, and strong Pb–X bonding.[48] This high strain tolerance[22,48,49] motivated the investigation of strain effects in this work. Strains ranging from −5% (compression) to 5% (tension) were applied to the

Fig. 1 Structures of FAPbI$_3$ for different phases.

optimized FAPbI$_3$ structure. To ensure structural reasonableness, atomic positions were fully relaxed with fixed lattice parameters. Average bond lengths, bond angles, and energies for the optimized structure are presented in Table S1 (ESI†). Bond length and bond angle variation trends are shown in Fig. S1 (ESI†). Compressive strain was found to enhance octahedral distortion, altering the Pb–I–Pb bond angles and reducing symmetry. These structural modifications directly correlate with changes in electronic and optical properties, as discussed in subsequent sections.

4. Results and discussion

4.1. Electronic properties

Bandgaps were calculated using multiple theoretical approaches. While the bandgaps calculated using the Perdew–Burke–Ernzerhof (PBE) functional are close to experimental values, this agreement is considered fortuitous.[50] When SOC is included, the bandgap of α-FAPbI$_3$ becomes significantly underestimated compared to experiments.[51,52] To improve accuracy, GW calculations incorporating SOC effects (G$_0$W$_0$) were employed, and the selected bandgap was determined to be 1.54 eV. The bandgaps obtained by different methods are presented in Table S2 (ESI†).

Previous studies show that α-FAPbI$_3$ thin films mainly adopt the (100) crystal plane orientation, which exhibits higher carrier mobility in this orientation.[53] However, (100) and (111) orientations are likely to coexist, with the (111) orientation demonstrating improved stability.[54,55] To study how strain affects different orientations, we applied −1% and 1% strains along the [100], [110], and [111] crystal orientations perpendicular to the (100), (110), and (111) planes, respectively (see Fig. S2, ESI†). Band structures and transition dipole moments were calculated, with results shown in Fig. 2. Under compressive strain, the bandgap progressively narrows, while tensile strain induces a widening trend, consistent with prior studies.[33,56] Bandgap changes primarily originate from shifts in the conduction band minimum (CBM), driven by enhanced orbital hybridization due to Pb–I bond contraction.[31,57,58] The bandgap exhibits minimal variation under strain along the [110] orientation, whereas the largest modulation occurs in the [111] orientation. When strain is applied along the [100] crystal orientation, tensile strain changes the band structure from direct to indirect bandgap. For strain application along the [110] orientation, both tensile and compressive strains induce indirect bandgap transitions. Only the [111] orientation maintains direct bandgap characteristics under strain. We further applied larger strains (up to 5% tensile/compressive) along the [111] orientation and calculated the band structure (Fig. S3, ESI†), confirming that the direct bandgap persists even under larger strain. Direct bandgaps enable electron transitions without phonon assistance, which enhances the performance of FAPbI$_3$ photovoltaic materials. The calculation of transition dipole moments reveals that, under compressive strain, the transition dipole moment exhibits an increasing trend, indicating an enhanced probability of electron transitions.[59,60]
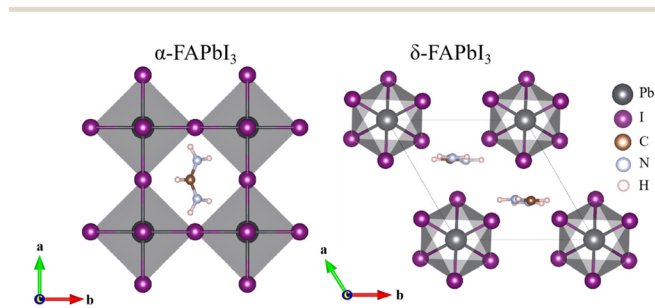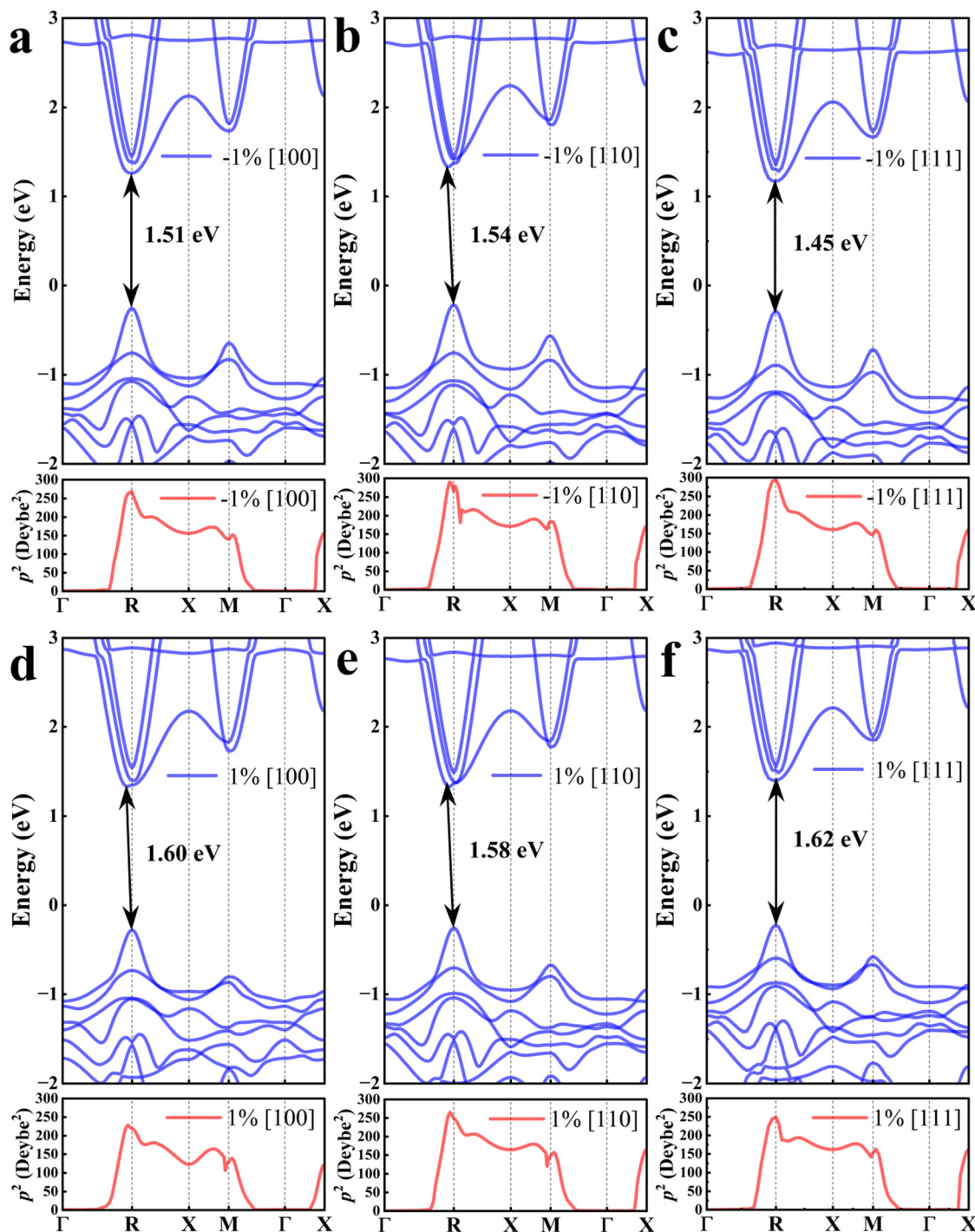
Fig. 2 (a)–(c) Band structures and transition dipole moments under 1% compressive strain applied along the [100], [110], and [111] crystal orientations; (d)–(f) the corresponding results under 1% tensile strain.

In summary, when strain is applied along the [111] crystal orientation, FAPbI$_3$ exhibits greater changes in band structure while maintaining a direct bandgap feature, which is highly favorable for band structure modulation. Consequently, we systematically investigated the strain-induced modifications in carrier dynamics and optical characteristics of the [111] crystal orientation.

4.2. Changes in properties under strain

4.2.1. Carrier behavior and optical properties. Fig. 3 shows the electron effective mass m_e^*, hole effective mass m_h^*, and exciton binding energy E_{eb} under different strains, and the specific values are presented in Table 1 (calculation details in the ESI,† S1.1) and polarizability values are shown in Table S3 (ESI†). As shown in Fig. 3, both m_e^* and m_h^* decrease under
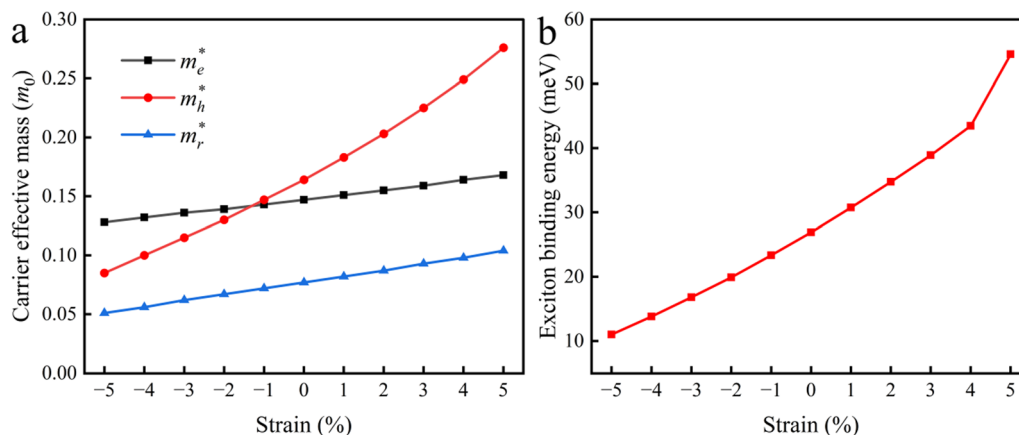
Fig. 3   (a) Carrier effective mass under different strains; (b) exciton binding energy.

Table 1   Computed carrier effective mass and exciton binding energy of FAPbI$_3$

Strain (%)	$m_{\mathrm{e}}^*(m_0)$	$m_{\mathrm{h}}^*(m_0)$	$m_{\mathrm{r}}^*(m_0)$	E_{eb} (meV)
−5	0.128	0.085	0.051	11.01
−4	0.132	0.100	0.056	13.81
−3	0.136	0.115	0.062	16.81
−2	0.139	0.130	0.067	19.91
−1	0.143	0.147	0.072	23.36
0	0.147	0.164	0.077	26.92
1	0.151	0.183	0.082	30.75
2	0.155	0.203	0.087	34.75
3	0.159	0.225	0.093	38.9
4	0.164	0.249	0.098	43.46
5	0.168	0.276	0.104	54.59

compressive strain but increase under tensile strain, governed by curvature changes in the valence band maximum (VBM) and CBM. Notably, m_{h}^* exhibits greater strain sensitivity due to stronger orbital hybridization and localization in the valence band (primarily Pb 6s and I 5p orbitals).[61,62]

Reduced effective mass under compression enhances carrier mobility, whereas tensile strain degrades transport properties,[61,63–66] which aligns well with findings reported in studies where compressive strain induces lattice contraction and significantly enhances hole mobility, facilitating charge transport.[18] The calculated E_{eb} values (11.01–54.59 meV) align with experimental reports for FAPbI$_3$ and MAPbI$_3$.[67–73] Strain-induced lattice distortions modulate E_{eb} through changes in dielectric constants and carrier effective mass. Elevated E_{eb} under tension impedes exciton dissociation, increasing recombination losses,[13,74,75] which is detrimental to photovoltaic performance.[76,77] However, enhanced E_{eb} may also enable narrower optical bandgaps and broader spectral response via excitonic absorption, potentially improving photocurrent generation.[78]

Optical properties were analyzed using dielectric functions (0–3 eV range, Fig. S4, ESI†). The absorption coefficient was calculated as shown in Fig. 4(a). Absorption edges blue-shift with tensile strain magnitude, indicating bandgap widening. Although the joint density of states (JDOS) shown in Fig. 4(c) is

reduced under compressive strain, the enhanced transition dipole moment increases the electron transition probability, ultimately still strengthening optical absorption.[79] Fig. 4(b) shows that the energy loss trends suggest trade-offs between light absorption enhancement and electron–phonon energy dissipation.[53,80]

The Shockley–Queisser (S–Q) method predicts photoelectric conversion efficiency (PCE) based solely on material bandgap while ignoring light absorption effects, prompting our use of the spectroscopic limited maximum efficiency (SLME) approach to address this limitation,[81,82] which incorporates absorption spectra, to predict more realistic PCE values as a function of material thickness. The predicted PCE is presented in Fig. 4(d). Since perovskite films in experimental studies are typically fabricated with a thickness of approximately 0.5 μm,[83] the PCE values corresponding to this thickness are listed in Table 2.

Under tensile strain, the PCE of FAPbI$_3$ is consistently lower than that of the unstrained system. Compressive strain initially enhances the PCE, but when compressive strain exceeds 2%, the PCE gradually decreases. At 5% compressive strain, the PCE becomes even lower than that in the unstrained case. This occurs because the Shockley–Queisser (S–Q) limit corresponds to an optimal bandgap of 1.34 eV, and excessive compressive strain further reduces the bandgap (as shown in Fig. S3, ESI†), deviating from this optimal value. In practical terms, when the bandgap becomes too small, the energy of incident photons is dissipated as heat. Combining these results with exciton binding energy calculations, the optimal compressive strain range for FAPbI$_3$ is determined to be −2% to −3%, which maximizes photovoltaic performance while avoiding efficiency losses.

4.2.2.   Defect properties. FAPbI$_3$ thin films in photovoltaic devices exhibit high defect densities ranging from 9.6×10^{15} to 1.37×10^{16} cm^{-3},[84] significantly exceeding those of conventional semiconductors (10^8 to 10^{15} cm^{-3}.[85–88]). While FAPbI$_3$ shows inherent defect tolerance,[8,89] suppressing defects remains critical for improving performance. Previous studies suggest that most defects in OIHPs form shallow traps with minimal impact on carrier transport.[90–92] However, interstitial
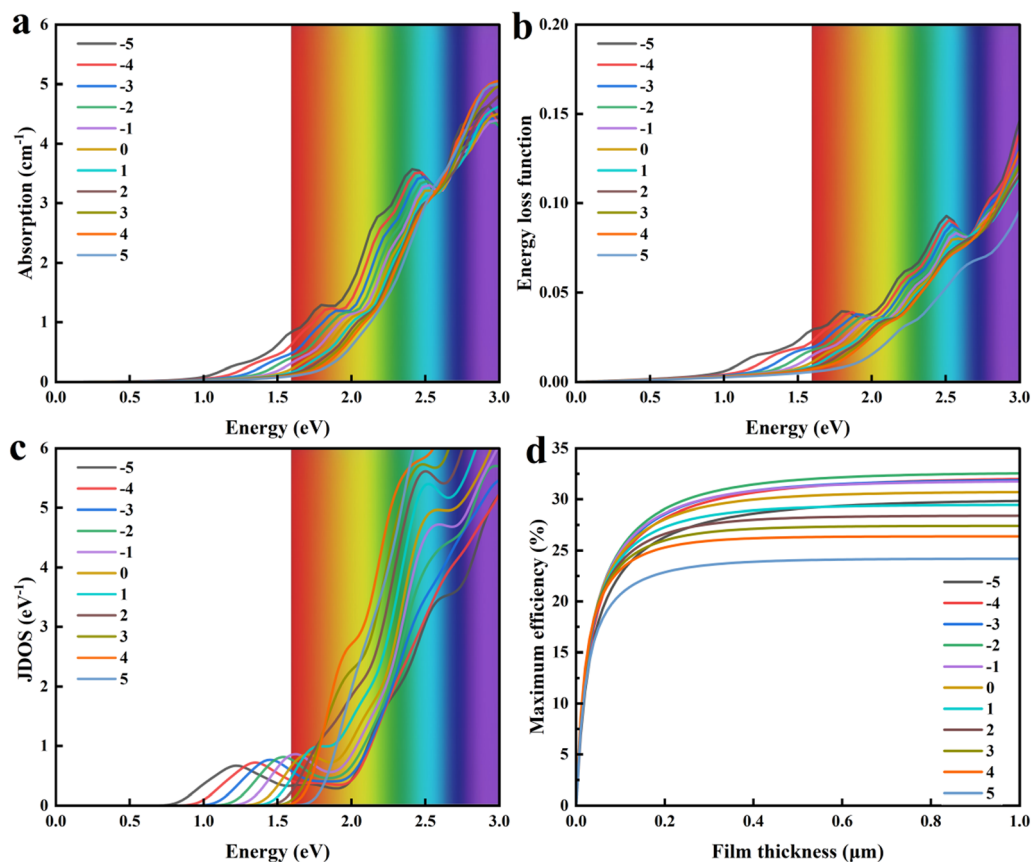
Fig. 4 (a) Absorption coefficient, (b) energy loss function, (c) joint density of states (JDOS), and (d) SLME of FAPbI$_3$ under varying strains.

Table 2 PCE of a 0.5 μm thick FAPbI$_3$ thin film predicted by SLME under different strains

Strain (%)	PCE (%)
−5	29.08
−4	31.16
−3	31.26
−2	31.90
−1	31.22
0	30.30
1	29.17
2	28.21
3	27.28
4	26.30
5	24.04

defects, particularly iodine interstitials, introduce deep-level traps within the bandgap, severely degrading carrier mobility.[93]

Fig. 5 shows the vacancy defect formation energy (DFE) under different strains (computational details in the ESI,† S1.4). Under compressive strain, the vacancy formation energies for iodine and lead increase, while tensile strain reduces them, suggesting compressive strain may decrease vacancy defect density. No trap levels occur within the bandgap under applied strains, indicating vacancy defect levels have minimal influence on carrier transition.

Fig. 6 illustrates the DFE and trap levels of iodine and lead interstitials under different strains. Under compressive strain, the DFE for both interstitials increases, indicating suppressed defect formation. For iodine interstitials in Fig. 6(a), deep-level traps in the unstrained case shift toward shallow levels near the VBM under compression, reducing carrier trapping and enabling ionization for optimized transport.[94–96] In Fig. 6(b), the thermodynamically stable (2+/0) trap level for lead interstitials under zero strain lies near the CBM. However, tensile strain induces a shift of the trap level toward the midgap region, which may lead to the formation of deep level traps. This enhances the carrier capture capability of the trap level and should be actively avoided.

In addition to defect formation energy (DFE) and trap levels, defect migration is critically important.[97] Higher migration rates may lead to perovskite phase separation or structural degradation.[53,98] Previous studies have demonstrated that iodine-related defects exhibit higher mobility compared to lead-related defects,[99,100] suggesting that iodine-related defects likely dominate migration processes.[101–103] To investigate interstitial defect migration under strain, supercells under compressive strain, tensile strain, and no strain were selected. Molecular dynamics simulations were conducted using the NVT ensemble (canonical ensemble) with a Langevin thermostat at 300 K,[104,105] employing a time step of 1 fs for a total
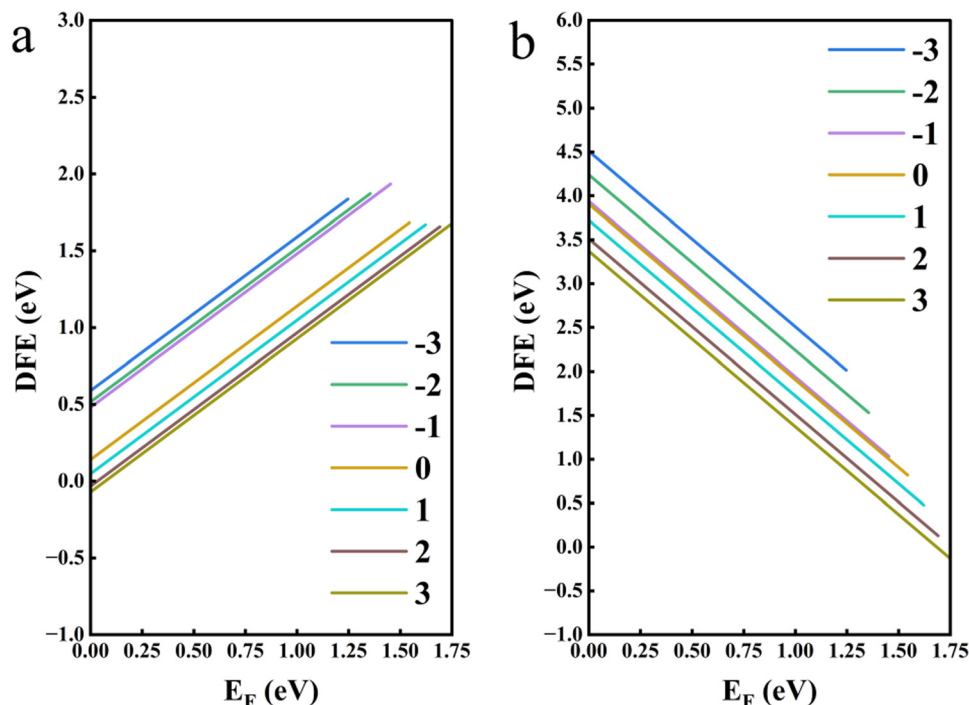
Fig. 5 (a) Iodine vacancy DFE and (b) lead vacancy DFE *versus* the Fermi energy and trap levels under different strains.

duration of 10 ps. To ensure accurate root-mean-square displacement (RMSD) calculations, RMSD values after an initial 5 ps equilibration period are shown in Fig. 7. The results clearly indicate that iodine interstitials exhibit significantly larger RMSD values compared to lead interstitials. Therefore, the focus was placed on iodine interstitials, and diffusion coefficients as well as ionic mobilities were calculated from the RMSD data (computational details in the ESI,† S1.5). These values are summarized in Table 3. Under compressive strain, both the diffusion coefficient and ionic mobility of iodine interstitials show a pronounced decrease, confirming that compressive strain effectively suppresses iodine interstitial migration.

Additional studies indicate that the presence of iodine interstitial defects facilitates the phase transition from the photoactive α-FAPbI$_3$ to the non-photoactive δ-FAPbI$_3$;[14] compared to the defect-free case, the energy barrier for phase transition with iodine interstitials is nearly halved, decreasing from 689 meV to 354 meV.[106] This occurs because the phase transition pathway involving iodine interstitials promotes atomic displacements, enabling rapid transformation from corner-sharing to face-sharing structures, accompanied by lower energy barriers and faster transition rates. In this study, we simulated the phase transition of α-FAPbI$_3$ and δ-FAPbI$_3$ with iodine interstitials under different strains, ensuring a one-to-one correspondence between initial and final atomic states. The phase transition barrier under zero strain as shown in Fig. 8 is 379 meV, consistent with previous studies.[106] As compressive strain increases, the energy barrier between the cubic and hexagonal phases gradually rises, reaching 668 meV

at −3% strain. In contrast, tensile strain reduces the phase transition barrier. Previous experiments have demonstrated that compressive strain can suppress the phase transition from α-FAPbI$_3$ to δ-FAPbI$_3$, maintaining the stability of FAPbI$_3$ at room temperature for over one year.[18] The calculations show that compressive strain plays a significant role in stabilizing the FAPbI$_3$ photoactive phase.

Compressive strain decreases interstitial defect density and converts deep-level traps into shallow-level ones in FAPbI$_3$ with interstitial defects, enhancing carrier transport. Simultaneously, diminished defect mobility and elevated phase transition barriers improve photoactive phase stability, ensuring long-term structural and functional stability.

4.2.3. Mechanical properties. The mechanical properties of FAPbI$_3$ are strongly correlated with defect behavior.[107] Mechanical parameters under different strains are shown in Fig. 9; as presented in Table 4, compressive strain significantly enhances lattice rigidity. The bulk modulus increases from 13.9 GPa (unstrained) to 28.45 GPa under −5% strain (105% increase), and the shear modulus increases from 4.29 GPa to 7.69 GPa (79% increase). These changes result from shortened Pb–I bond lengths (Table S1, ESI†) and increased octahedral distortion, which improve resistance to shear strain. Young's modulus increases from 11.68 GPa (unstrained) to 21.28 GPa (−5% strain), indicating reduced elastic deformability under compression. Studies suggest that a higher Young's modulus elevates ion migration barriers, suppressing ion motion at grain boundaries and reducing trap-state density.[108,109]

Notably, the strain dependence of mechanical properties is nonlinear. Beyond −3% compressive strain, the rates of
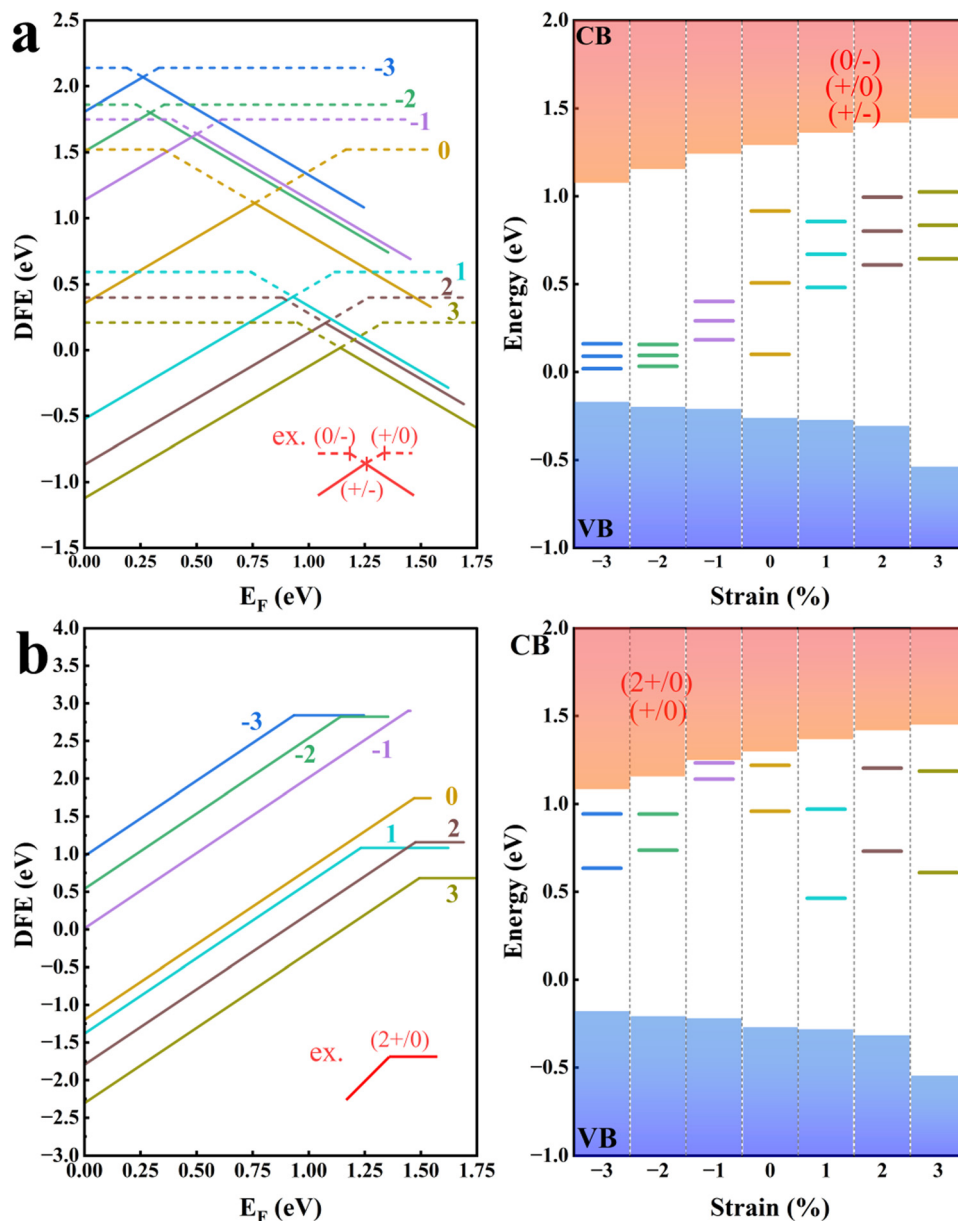
Fig. 6 (a) DFE of iodine interstitials under different strains as a function of the Fermi energy and the corresponding trap-levels; (b) DFE of lead interstitials under different strains as a function of the Fermi energy and the corresponding trap-levels.

increase in bulk and shear moduli are slow, suggesting proximity to the elastic limit.[80] Under 5% tensile strain, Young's modulus plummets to 3.6 GPa (83% reduction), reflecting severe lattice softening due to elongated Pb–I bonds. This softening correlates with enhanced iodine interstitial mobility (Table 3) and reduced phase transition barriers (Fig. 8).

Poisson's ratio is slightly higher under compression (0.36 to 0.38), indicating dominant transverse expansion that may relieve lattice strain. Lower Poisson's ratio under tension (0.34 to 0.36) suggests axial elongation-driven deformation, exacerbating lattice anisotropy.[110,111]

In summary, compressive strain enhances lattice rigidity (high bulk/shear moduli) and suppresses deformation (high Young's modulus), synergistically reducing defect migration

and phase instability. Conversely, tensile strain softens the lattice, accelerating defect dynamics. These findings establish a mechano-defect coupling mechanism, providing a theoretical basis for designing stable FAPbI$_3$-based photovoltaics.

5. Conclusion

Through first-principles calculations, this study systematically investigates strain effects on the optoelectronic properties, defect behavior, and mechanical performance of α-FAPbI$_3$. The [111] orientation maintains direct bandgap characteristics under strain, while [100] and [110] orientations exhibit indirect bandgap transitions under tensile strain. Moderate
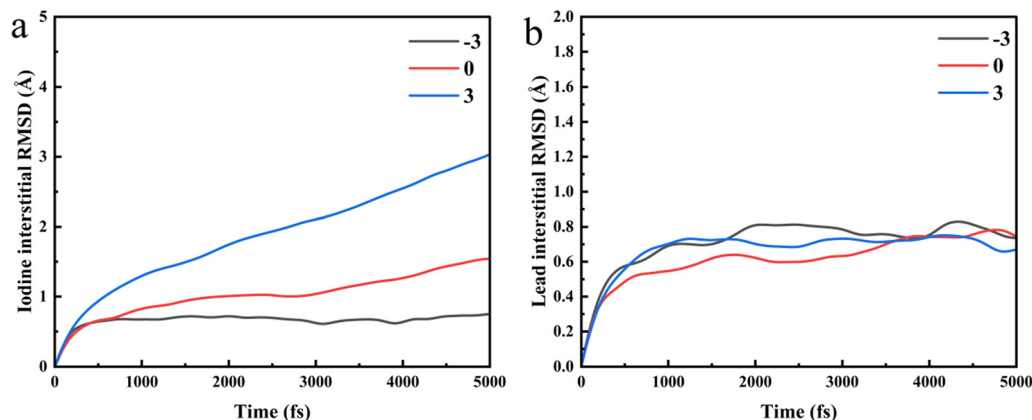
Fig. 7 (a) RMSD of iodine interstitials and (b) lead interstitials under different strains.

Table 3 The diffusion coefficient and ion mobility obtained through molecular dynamics calculations

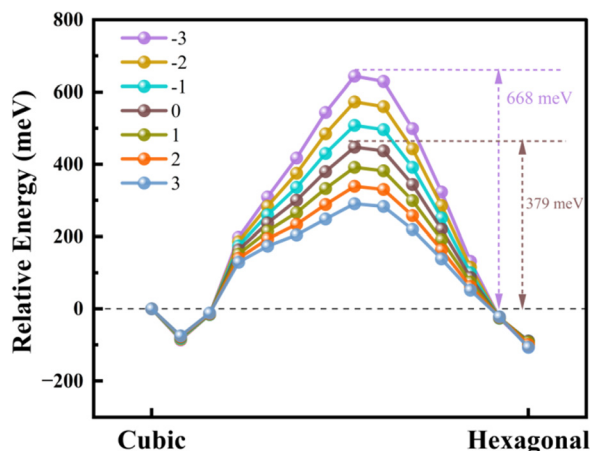| Strain (%)	Diffusion coefficient (cm^2 s^{-1})	Ionic mobility (absolute value) (cm^2 V^{-1} s^{-1})
−3	0.275×10^{-5}	0.106×10^{-3}
0	0.818×10^{-5}	0.316×10^{-3}
3	0.244×10^{-4}	0.945×10^{-3}

Fig. 8 Energy barrier for the phase transition of FAPbI$_3$ between the cubic (α-FAPbI$_3$) and hexagonal (δ-FAPbI$_3$) phases under varying strain conditions.

Fig. 9 Calculated mechanical parameters under different strains.

Table 4 Calculated mechanical parameters under different strains

Strain (%)	Bulk modulus (GPa)	Young's modulus (GPa)	Shear modulus (GPa)	Poisson's ratio
−5	28.45	21.18	7.69	0.38
−4	25.22	20.94	7.69	0.36
−3	19.50	14.00	5.07	0.38
−2	18.01	12.97	4.70	0.38
−1	16.25	12.66	4.62	0.37
0	13.90	11.68	4.29	0.36
1	10.75	10.34	3.86	0.34
2	10.74	9.22	3.40	0.36
3	9.30	8.93	3.33	0.34
4	8.40	7.56	2.80	0.35
5	4.28	3.60	1.32	0.36

compressive strain (−2% to −3%) optimizes the bandgap to the Shockley–Queisser ideal value (∼1.34 eV) while reducing exciton binding energy and carrier effective mass. Compressive strain suppresses deep-level defects by increasing defect formation energy and migration barriers while stabilizing the photoactive phase through elevating the α-FAPbI$_3$ to δ-FAPbI$_3$ phase transition barrier to 668 meV. Molecular dynamics simulations confirm reduced iodine interstitial diffusion coefficients under compression, effectively inhibiting ion migration. Mechanical analysis reveals compressive strain enhances
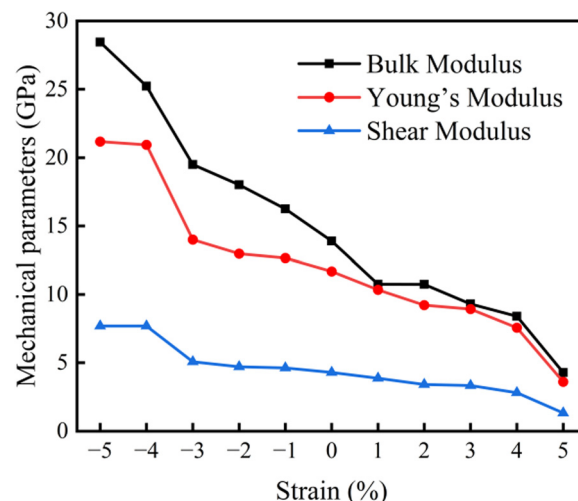
the bulk modulus and shear modulus, improving lattice rigidity, whereas tensile strain induces lattice softening and accelerates defect dynamics. By integrating crystal orientation control and interfacial stress regulation, the [111] orientation under −2% strain achieves a 31.9% photoelectric conversion

efficiency, providing a theoretical foundation and design strategy for synergistic optimization of stability and efficiency in perovskite solar cells.

Author contributions

Jiaqi Dai: writing – original draft, methodology, formal analysis, data curation. Xiaoshan Wu: writing – review & editing, resources, methodology, funding acquisition, formal analysis. Tingfeng Li: methodology, investigation. Xiaolei Li: formal analysis, methodology, software. Cuiping Xu: investigation. Min Zhao: resources. Hongling Cai: writing – review & editing, funding acquisition, formal analysis, data curation.

Conflicts of interest

There are no conflicts to declare.

Data availability

The data that support the findings of this study are available within the article and its ESI.†

Acknowledgements

References

1 Y. Zhang, Y. Chen, G. Liu, Y. Wu, Z. Guo, R. Fan, K. Li, H. Liu, Y. Zhao, T. Kodalle, Y. Chen, C. Zhu, Y. Bai, Q. Chen and H. Zhou, *Science*, 2025, **387**, 284–290.

2 J. Burschka, N. Pellet, S. J. Moon, R. Humphry-Baker, P. Gao, M. K. Nazeeruddin and M. Gratzel, *Nature*, 2013, **499**, 316–319.

3 W. Zuo, W. Fu, K. Wang, C. Das, M. M. Byranvand, K.-L. Wang, A. Chaudhary, J. Lim, M. Li and M. Saliba, *Energy Environ. Sci.*, 2024, **17**, 1407–1415.

4 J. Jiang, R. Pachter, C.-K. Lim, J. E. Haley and P. N. Prasad, *J. Phys. Chem. C*, 2020, **124**, 3224–3232.

5 J. Liu, H. Zhang, J. Wang and X. Zong, *J. Mater. Chem. A*, 2024, **12**, 5740–5747.

6 J. Feng, C. H. Mak, L. Yu, B. Han, H. H. Shen, S. P. Santoso, M. Yuan, F. F. Li, H. Song, J. C. Colmenares and H. Y. Hsu, *Small Methods*, 2023, **8**, 2300429.

7 J. Xie, W. Zhou, H. Li, Z. Wang, J. Jiang, Y. Zhang, X. Shen, Z. Ning and W. Liu, *Adv. Opt. Mater.*, 2024, **12**, 2303004.

8 Z. W. Gao, Y. Wang, H. Liu, J. Sun, J. Kim, Y. Li, B. Xu and W. C. H. Choy, *Adv. Funct. Mater.*, 2021, **31**, 2101438.

9 X. Huang, L. Bi, Z. Yao, Q. Fu, B. Fan, S. Wu, Z. Su, Q. Feng, J. Wang, Y. Hong, M. Liu, Y. An, M. Chen and A. K. Y. Jen, *Adv. Mater.*, 2024, **36**, 2410564.

10 P. Zhu, C. Chen, J. Dai, Y. Zhang, R. Mao, S. Chen, J. Huang and J. Zhu, *Adv. Mater.*, 2024, **36**, 2307357.

11 X. Li, D. Bi, C. Yi, J.-D. Décoppet, J. Luo, S. M. Zakeeruddin, A. Hagfeldt and M. Grätzel, *Science*, 2016, **353**, 58–62.

12 H. Gu, A. Zhu, J. Xia, W. Li, J. Zheng, T. Yang, S. Li, N. Zhang, S. Mei, Y. Cai, S. Chen, C. Liang and G. Xing, *Sci. Bull.*, 2024, **69**, 2853–2861.

13 Y. Meng, Y. Wang, C. Liu, P. Yan, K. Sun, Y. Wang, R. Tian, R. Cao, J. Zhu, H. Do, J. Lu and Z. Ge, *Adv. Mater.*, 2023, **36**, 2309208.

14 H. S. Kim and N. G. Park, *Adv. Energy Mater.*, 2024, **15**, 2400089.

15 K. Galkowski, A. Mitioglu, A. Miyata, P. Plochocka, O. Portugall, G. E. Eperon, J. T.-W. Wang, T. Stergiopoulos, S. D. Stranks, H. J. Snaith and R. J. Nicholas, *Energy Environ. Sci.*, 2016, **9**, 962–970.

16 M. Bokdam, T. Sander, A. Stroppa, S. Picozzi, D. D. Sarma, C. Franchini and G. Kresse, *Sci. Rep.*, 2016, **6**, 28618.

17 Y. Liu, C. Tao, Y. Cao, L. Chen, S. Wang, P. Li, C. Wang, C. Liu, F. Ye, S. Hu, M. Xiao, Z. Gao, P. Gui, F. Yao, K. Dong, J. Li, X. Hu, H. Cong, S. Jia, T. Wang, J. Wang, G. Li, W. Huang, W. Ke, J. Wang and G. Fang, *Nat. Commun.*, 2022, **13**, 7425.

18 Y. Chen, Y. Lei, Y. Li, Y. Yu, J. Cai, M. H. Chiu, R. Rao, Y. Gu, C. Wang, W. Choi, H. Hu, C. Wang, Y. Li, J. Song, J. Zhang, B. Qi, M. Lin, Z. Zhang, A. E. Islam, B. Maruyama, S. Dayeh, L. J. Li, K. Yang, Y. H. Lo and S. Xu, *Nature*, 2020, **577**, 209–215.

19 S. Huang, Y. Wu, G. Xu, Y. Shen, W. Liu, J. Xu, T. Xu, T. Wu, Z. Cao and Y. Li, *Adv. Funct. Mater.*, 2025, **35**, 2418777.

20 S. Porwal, N. K. Bansal, S. Ghosh and T. Singh, *Energy Adv.*, 2024, **3**, 894–903.

21 N. Rolston, K. A. Bush, A. D. Printz, A. Gold-Parker, Y. Ding, M. F. Toney, M. D. McGehee and R. H. Dauskardt, *Adv. Energy Mater.*, 2018, **8**, 1802139.

22 J. Zhao, Y. Deng, H. Wei, X. Zheng, Z. Yu, Y. Shao, J. E. Shield and J. Huang, *Sci. Adv.*, 2017, **3**, eaao5616.

23 Y. Yang, Y. Wang, Z. Qu, K. Zhang, T. Liang, S. Chen, W. Lv, F. Min, Y. Chen, Y. Qiao and Y. Song, *Angew. Chem., Int. Ed.*, 2023, **62**, 2300971.

24 M. Tao, Y. Wang, K. Zhang, Z. Song, Y. Lan, H. Guo, L. Guo, X. Zhang, J. Wei, D. Cao and Y. Song, *Joule*, 2024, **8**, 3142–3152.

25 L. Zheng, M. Wei, F. T. Eickemeyer, J. Gao, B. Huang, U. Gunes, P. Schouwink, D. W. Bi, V. Carnevali, M. Mensi, F. Biasoni, Y. Zhang, L. Agosta, V. Slama, N. Lempesis, M. A. Hope, S. M. Zakeeruddin, L. Emsley, U. Rothlisberger, L. Pfeifer, Y. Xuan and M. Grätzel, *Science*, 2025, **388**, 88–95.

26 X. Zhang, *Matter*, 2020, **2**, 294–296.

27 K. Li and H. Zhou, *Chin. J. Chem.*, 2023, **41**, 2730–2745.

28 Y. Shen, T. Zhang, G. Xu, J. A. Steele, X. Chen, W. Chen, G. Zheng, J. Li, B. Guo, H. Yang, Y. Wu, X. Lin, T. Alshahrani, W. Yin, J. Zhu, F. Wang, A. Amassian, X. Gao, X. Zhang, F. Gao, Y. Li and Y. Li, *Nature*, 2024, **635**, 882–889.

29 D. W. de Quilettes, S. M. Vorpahl, S. D. Stranks, H. Nagaoka, G. E. Eperon, M. E. Ziffer, H. J. Snaith and D. S. Ginger, *Science*, 2015, **348**, 683–686.

30 Y. Yin, X. Yan, H. Luo, Y. Liang, P. Xu, Y. Wang, S. Jin and W. Tian, *Angew. Chem., Int. Ed.*, 2024, **64**, 2418587.

31 Y. Wang, X. Sun, T. Shao, D. Zhao, L. Zhang, Y. Li, Q. Dong, C. Liu, K. Wang, G. Xiao and B. Zou, *Inorg. Chem.*, 2024, **63**, 11431–11437.

32 A. S. Subbiah, S. Mannar, V. Hnapovskyi, A. R. Pininti, B. Vishal, L. V. Torres Merino, O. Matiash, O. Karalis, H. Hempel, A. Prasetio, B. Yildirim, P. Dally, D. Rosas Villalva, M. Babics, L. Xu, A. Razzaq, R. Azmi, F. Xu, H. L. Bristow, E. Ugur, A. Ur Rehman, H. Pasanen, E. Aydin, T. Allen, D. Baran, T. Unold, F. Laquai and S. De Wolf, *Joule*, 2025, **9**, 101767.

33 F. Mahajabin, M. R. Islam, M. M. Masud and M. M. Rahman, *Mater. Chem. Phys.*, 2024, **313**, 128763.

34 X. Ma, W.-H. Fang, R. Long and O. V. Prezhdo, *J. Am. Chem. Soc.*, 2024, **146**, 16314–16323.

35 G. Kresse and J. Furthmüller, *Comput. Mater. Sci.*, 1996, **6**, 15–50.

36 G. Kresse and J. Furthmüller, *Phys. Rev. B: Condens. Matter Mater. Phys.*, 1996, **54**, 11169–11186.

37 P. E. Blöchl, *Phys. Rev. B: Condens. Matter Mater. Phys.*, 1994, **50**, 17953–17979.

38 J. P. Perdew, K. Burke and M. Ernzerhof, *Phys. Rev. Lett.*, 1996, **77**, 3865–3868.

39 O. J. Weber, D. Ghosh, S. Gaines, P. F. Henry, A. B. Walker, M. S. Islam and M. T. Weller, *Chem. Mater.*, 2018, **30**, 3768–3778.

40 M. Shishkin and G. Kresse, *Phys. Rev. B: Condens. Matter Mater. Phys.*, 2007, **75**, 235102.

41 J. Lim, M. T. Hörantner, N. Sakai, J. M. Ball, S. Mahesh, N. K. Noel, Y.-H. Lin, J. B. Patel, D. P. McMeekin, M. B. Johnston, B. Wenger and H. J. Snaith, *Energy Environ. Sci.*, 2019, **12**, 169–176.

42 M. van Schilfgaarde, T. Kotani and S. Faleev, *Phys. Rev. Lett.*, 2006, **96**, 226402.

43 M. L. Tiago and J. R. Chelikowsky, *Phys. Rev. B: Condens. Matter Mater. Phys.*, 2006, **73**, 205334.

44 G. Onida, L. Reining and A. Rubio, *Rev. Mod. Phys.*, 2002, **74**, 601–659.

45 V. Wang, N. Xu, J.-C. Liu, G. Tang and W.-T. Geng, *Comput. Phys. Commun.*, 2021, **267**, 108033.

46 M. T. Weller, O. J. Weber, J. M. Frost and A. Walsh, *J. Phys. Chem. Lett.*, 2015, **6**, 3209–3212.

47 T. Chen, W.-L. Chen, B. J. Foley, J. Lee, J. P. C. Ruff, J. Y. P. Ko, C. M. Brown, L. W. Harriger, D. Zhang, C. Park, M. Yoon, Y.-M. Chang, J. J. Choi and S.-H. Lee, *Proc. Natl. Acad. Sci. U. S. A.*, 2017, **114**, 7519–7524.

48 X. Li, Y. Meng, W. Li, J. Zhang, C. Dang, H. Wang, S.-W. Hung, R. Fan, F.-R. Chen, S. Zhao, J. C. Ho and Y. Lu, *Nat. Mater.*, 2023, **22**, 1175–1181.

49 J. Zhang, C. Xie, G. Li, P. Dai, L. Yang, R. Liu and B. Pan, *J. Chem. Phys.*, 2019, **151**, 134104.

50 P. Umari, E. Mosconi and F. De Angelis, *Sci. Rep.*, 2014, **4**, 4467.

51 J. Even, L. Pedesseau, J.-M. Jancu and C. Katan, *J. Phys. Chem. Lett.*, 2013, **4**, 2999–3005.

52 L.-K. Gao, Y.-L. Tang and X.-F. Diao, *Mater. Res. Express*, 2020, **7**, 116201.

53 P. Shi, Y. Ding, B. Ding, Q. Xing, T. Kodalle, C. M. Sutter-Fella, I. Yavuz, C. Yao, W. Fan, J. Xu, Y. Tian, D. Gu, K. Zhao, S. Tan, X. Zhang, L. Yao, P. J. Dyson, J. L. Slack, D. Yang, J. Xue, M. K. Nazeeruddin, Y. Yang and R. Wang, *Nature*, 2023, **620**, 323–327.

54 X. Liu, X. Jiang, Y. Yin, J. Zhang, H. Tian, J. Guo, X. Guo and C. Li, *Energy Environ. Sci.*, 2024, **17**, 6058–6067.

55 T. Yang, Y. Yang, T. Niu, E. Zhao, N. Wu, S. Wang, X. Chen, S. Wang, Y. Wang, Y. Wu, Z. Zhang, C. Ma, Y. Gong, D. Liu and K. Zhao, *ACS Energy Lett.*, 2024, **10**, 427–438.

56 J. Jin, Z. Zhang, S. Zou, F. Cao, Y. Huang, Y. Jiang, Z. Gao, Y. Xu, J. Qu, X. Wang, C. Chen, C. Xiao, S. Ren and D. Zhao, *Adv. Energy Mater.*, 2024, **15**, 2403718.

57 S. Sidhik, I. Metcalf, W. Li, T. Kodalle, C. J. Dolan, M. Khalili, J. Hou, F. Mandani, A. Torma, H. Zhang, R. Garai, J. Persaud, A. Marciel, I. A. Muro Puente, G. N. M. Reddy, A. Balvanz, M. A. Alam, C. Katan, E. Tsai, D. Ginger, D. P. Fenning, M. G. Kanatzidis, C. M. Sutter-Fella, J. Even and A. D. Mohite, *Science*, 2024, **384**, 1227–1235.

58 R. Wang, X. Li, J. Qi, C. Su, J. Yang, S. Yang, M. Yuan and T. He, *Adv. Mater.*, 2023, **35**, 2304149.

59 Y. Tang, Q. Xie, X. Zhang, J. Ma, H. Xie, Y. Liu, L. Zhao, D. Yan, X. Wang and W. Ye, *Laser Photonics Rev.*, 2025, 2500430.

60 J. Cui, Y. Liu, Y. Deng, C. Lin, Z. Fang, C. Xiang, P. Bai, K. Du, X. Zuo, K. Wen, S. Gong, H. He, Z. Ye, Y. Gao, H. Tian, B. Zhao, J. Wang and Y. Jin, *Sci. Adv.*, 2021, **7**, eabg8458.

61 Z. Muhammad, P. Liu, R. Ahmad, S. Jalali-Asadabadi, C. Franchini and I. Ahmad, *AIP Adv.*, 2022, **12**, 025330.

62 S. Tan, T. Huang, I. Yavuz, R. Wang, T. W. Yoon, M. Xu, Q. Xing, K. Park, D.-K. Lee, C.-H. Chen, R. Zheng, T. Yoon, Y. Zhao, H.-C. Wang, D. Meng, J. Xue, Y. J. Song, X. Pan, N.-G. Park, J.-W. Lee and Y. Yang, *Nature*, 2022, **605**, 268–273.

63 E. Menéndez-Proupin, P. Palacios, P. Wahnón and J. C. Conesa, *Phys. Rev. B: Condens. Matter Mater. Phys.*, 2014, **90**, 045207.

64 R. Ben Aich, S. Ben Radhia, K. Boujdaria, M. Chamarro and C. Testelin, *J. Phys. Chem. Lett.*, 2020, **11**, 808–817.

65 D. Chu, B. Jia, N. Liu, Y. Zhang, X. Li, J. Feng, J. Pi, Z. Yang, G. Zhao, Y. Liu, S. Liu and N.-G. Park, *Sci. Adv.*, 2023, **9**, eadh2255.

66 L. Zhao, Y. Zhou, Z. Shi, Z. Ni, M. Wang, Y. Liu and J. Huang, *Nat. Photonics*, 2023, **17**, 315–323.

67 V. D'Innocenzo, G. Grancini, M. J. P. Alcocer, A. R. S. Kandada, S. D. Stranks, M. M. Lee, G. Lanzani, H. J. Snaith and A. Petrozza, *Nat. Commun.*, 2014, **5**, 3586.

68 Q. Lin, A. Armin, R. C. R. Nagiri, P. L. Burn and P. Meredith, *Nat. Photonics*, 2014, **9**, 106–112.

69 G. Grancini, A. R. Srimath Kandada, J. M. Frost, A. J. Barker, M. De Bastiani, M. Gandini, S. Marras, G. Lanzani, A. Walsh and A. Petrozza, *Nat. Photonics*, 2015, **9**, 695–701.

70 L. M. Herz, *Annu. Rev. Phys. Chem.*, 2016, **67**, 65–89.

PCCP

Paper

71 Y. Jiang, X. Wang and A. Pan, *Adv. Mater.*, 2019, **31**, 1806671.

72 A. Miyata, A. Mitioglu, P. Plochocka, O. Portugall, J. T.-W. Wang, S. D. Stranks, H. J. Snaith and R. J. Nicholas, *Nat. Phys.*, 2015, **11**, 582–587.

73 M. Saba, M. Cadelano, D. Marongiu, F. Chen, V. Sarritzu, N. Sestu, C. Figus, M. Aresti, R. Piras, A. Geddo Lehmann, C. Cannas, A. Musinu, F. Quochi, A. Mura and G. Bongiovanni, *Nat. Commun.*, 2014, **5**, 5049.

74 L. Cheng, B. Xu, X. Li, Y. Zeng and L. Meng, *ACS Appl. Energy Mater.*, 2022, **5**, 2430–2441.

75 F. Zhang, X. Zhang, C. Wang, M. Sun, X. Luo, Y. Yang, S. Chang, D. Zhang and L. Duan, *Nano Energy*, 2021, **79**, 105486.

76 H. Zhang, R. Wang, L. Yang, Z. Hu, H. Liu and Y. Liu, *Angew. Chem., Int. Ed.*, 2024, **63**, 2318206.

77 T. Zhou, Q. Li and L. Zhou, *Adv. Energy Mater.*, 2024, **14**, 2400050.

78 B. Li, Y. Yao, C. Kan, P. Hang, J. Xie, Q. Yin, D. Zhang, X. Yu and D. Yang, *Joule*, 2025, **9**, 012.

79 B. Yang, Z. Zhang, P. Liu, X. Fu, J. Wang, Y. Cao, R. Tang, X. Du, W. Chen, S. Li, H. Yan, Z. Li, X. Zhao, G. Qin, X.-Q. Chen and L. Zuo, *Nature*, 2023, **622**, 499–506.

80 H. Zhang, Z. Chen, M. Qin, Z. Ren, K. Liu, J. Huang, D. Shen, Z. Wu, Y. Zhang, J. Hao, C. S. Lee, X. Lu, Z. Zheng, W. Yu and G. Li, *Adv. Mater.*, 2021, **33**, 2008487.

81 R. Mayengbam, S. K. Tripathy and G. Palai, *Mater. Today Commun.*, 2020, **24**, 101216.

82 Y. Liu, J. Qian, H. Zhang, B. Xu, Y. Zhang, L. Liu, G. Chen and W. Tian, *Org. Electron.*, 2018, **62**, 269–276.

83 K. C. Dubey, A. Srivastava, N. Wadhwani and R. K. Shukla, *J. Electron. Mater.*, 2025, **54**, 1851–1878.

84 X. Zhu, C. Wang, C. Zhang, Z. Wang, J. Feng, S. Liu and D. Yang, *Chem. Eng. J.*, 2022, **434**, 134759.

85 T. Ueki, M. Itsumi and T. Takeda, *Appl. Phys. Lett.*, 1997, **70**, 1248–1250.

86 J. R. Ayres, *J. Appl. Phys.*, 1993, **74**, 1787–1792.

87 A. Balcioglu, R. K. Ahrenkiel and F. Hasoon, *J. Appl. Phys.*, 2000, **88**, 7175–7178.

88 L. L. Kerr, S. S. Li, S. W. Johnston, T. J. Anderson, O. D. Crisalle, W. K. Kim, J. Abushama and R. N. Noufi, *Solid-State Electron.*, 2004, **48**, 1579–1586.

89 A. Buin, R. Comin, J. Xu, A. H. Ip and E. H. Sargent, *Chem. Mater.*, 2015, **27**, 4405–4412.

90 E. Sezen, S. M. Oner, C. Deger and I. Yavuz, *J. Phys. Chem. Lett.*, 2022, **13**, 9718–9724.

91 N. Liu and C. Yam, *Phys. Chem. Chem. Phys.*, 2018, **20**, 6800–6804.

92 D. Meggiolaro and F. De Angelis, *ACS Energy Lett.*, 2018, **3**, 2206–2222.

93 D. Meggiolaro, S. G. Motti, E. Mosconi, A. J. Barker, J. Ball, C. Andrea Riccardo Perini, F. Deschler, A. Petrozza and F. De Angelis, *Energy Environ. Sci.*, 2018, **11**, 702–713.

94 L. Rubaldo, A. Brunner, J. Berthoz, N. Péré-Laperne, A. Kerlain, P. Abraham, D. Bauza, G. Reimbold and O. Gravrand, *J. Electron. Mater.*, 2014, **43**, 3065–3069.

95 G.-J. Zhu, J.-H. Yang and X.-G. Gong, *Phys. Rev. B: Condens. Matter Mater. Phys.*, 2020, **102**, 035202.

96 Z. Zhu, K. Mao, K. Zhang, W. Peng, J. Zhang, H. Meng, S. Cheng, T. Li, H. Lin, Q. Chen, X. Wu and J. Xu, *Joule*, 2022, **6**, 2849–2868.

97 C. Freysoldt, B. Grabowski, T. Hickel, J. Neugebauer, G. Kresse, A. Janotti and C. G. Van de Walle, *Rev. Mod. Phys.*, 2014, **86**, 253–305.

98 Y. Zhang, T. Kong, Y. Liu, X. Liu, W. Liu, M. Saliba and D. Bi, *Adv. Funct. Mater.*, 2024, **34**, 2401391.

99 X. Ren, J. Wang, Y. Lin, Y. Wang, H. Xie, H. Huang, B. Yang, Y. Yan, Y. Gao, J. He, J. Huang and Y. Yuan, *Nat. Mater.*, 2024, **23**, 810–817.

100 C. Eames, J. M. Frost, P. R. Barnes, B. C. O'Regan, A. Walsh and M. S. Islam, *Nat. Commun.*, 2015, **6**, 7497.

101 J. M. Azpiroz, E. Mosconi, J. Bisquert and F. De Angelis, *Energy Environ. Sci.*, 2015, **8**, 2118–2127.

102 J.-H. Yang, W.-J. Yin, J.-S. Park and S.-H. Wei, *J. Mater. Chem. A*, 2016, **4**, 13105–13112.

103 V. Adinolfi, M. Yuan, R. Comin, E. S. Thibau, D. Shi, M. I. Saidaminov, P. Kanjanaboos, D. Kopilovic, S. Hoogland, Z. H. Lu, O. M. Bakr and E. H. Sargent, *Adv. Mater.*, 2016, **28**, 3406–3410.

104 W. G. Hoover, A. J. C. Ladd and B. Moran, *Phys. Rev. Lett.*, 1982, **48**, 1818–1820.

105 D. J. Evans, *J. Chem. Phys.*, 1983, **78**, 3297–3302.

106 S. Tan, I. Yavuz, M. H. Weber, T. Huang, C.-H. Chen, R. Wang, H.-C. Wang, J. H. Ko, S. Nuryyeva, J. Xue, Y. Zhao, K.-H. Wei, J.-W. Lee and Y. Yang, *Joule*, 2020, **4**, 2426–2442.

107 J. Dai, W. Tang, T. Li, C. Xu, M. Zhao, P. Ji, X. Li, F. Zhang, H. Cai and X. Wu, *Nanomaterials*, 2025, **15**, 981.

108 Z. Wang, S. Tie, H. Zhang, C. Wan, Z. Liang, H. Xu, X. Zheng, W. Zhang, D. Aldakov, P. Reiss, J. Ye and X. Pan, *ACS Nano*, 2023, **17**, 13638–13647.

109 Z. Liang, J. Cao, Z. Zhou, L. Ren, H. Wu, Z. Wang, C. Yi, D. Yang, K. Wang and C. Wu, *Nat. Synth.*, 2025, **4**, 347–358.

110 Q. Pan, M. Yang, R. Feng, A. C. Chuang, K. An, P. K. Liaw, X. Wu, N. Tao and L. Lu, *Science*, 2023, **382**, 185–190.

111 W. Su, M. Wang, F. Guo, H. Ran, Q. Cheng, Q. Wang, Y. Zhu, X. Ma and C. Huang, *Acta Mater.*, 2024, **273**, 119982.